ACS Partner Journal

CHEMICAL & BIOMEDICAL IMAGING

pubs.acs.org/ChemBioImaging

Article

Real-Time Visualization of Endogenous H_2O_2 Production in Mammalian Spheroids by Electrochemiluminescence

Vanshika Gupta,[‖] Francesco Falciani,[‖] Brady R. Layman,[‖] Megan L. Hill, Stefania Rapino,* and Jeffrey E. Dick*

Cite This: *Chem. Biomed. Imaging* 2025, 3, 310−321

Read Online

ACCESS | Metrics & More | Article Recommendations | Supporting Information

ABSTRACT: Two-dimensional cell culture may be insufficient when it comes to understanding human disease. The redox behavior of complex, three-dimensional tissue is critical to understanding disease genesis and propagation. Unfortunately, few measurement tools are available for such three-dimensional models to yield quantitative insight into how reactive oxygen species (ROS) form over time. Here, we demonstrate an imaging platform for the real-time visualization of H_2O_2 formation for mammalian spheroids made of noncancerous human embryonic kidney cells (HEK-293) and metastatic breast cancer cells (MCF-7 and MDA-MB-231). We take advantage of the luminol and H_2O_2 electrochemiluminescence reaction on a transparent tin-doped indium oxide electrode. The luminescence of this reaction as a function of $[H_2O_2]$ is linear ($R^2 = 0.98$) with a dynamic range between 0.5 μM to 0.1 mM, and limit of detection of 2.26 ± 0.58 μM. Our method allows for the observation of ROS activity in growing spheroids days in advance of current techniques without the need to sacrifice the sample postanalysis. Finally, we use our procedure to demonstrate how key ROS pathways in cancerous spheroids can be up-regulated and downregulated through the addition of common metabolic drugs, rotenone and carbonyl cyanide-*p*-trifluoromethoxyphenylhydrazone. Our results suggest that the Warburg Effect can be studied for single mammalian cancerous spheroids, and the use of metabolic drugs allows one to implicate specific metabolic pathways in ROS formation. We expect this diagnostic tool to have wide applications in understanding the real-time propagation of human disease in a system more closely related to human tissue.

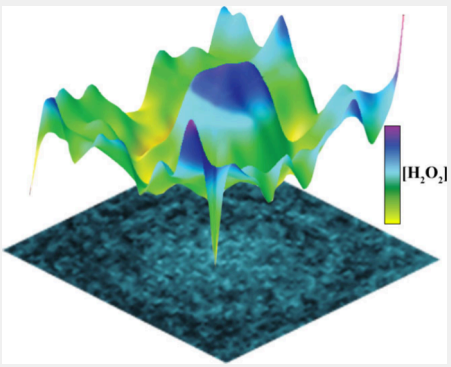

KEYWORDS: *electrochemiluminescence, luminol, cell spheroids, real-time analysis, peroxide production*

INTRODUCTION

Cultivation of animal cells in two-dimensional cultures was first demonstrated by Harrison in the early 1990s in a pivotal set of experiments where he isolated neuronal fibroblasts from the cochlea of tadpoles and tracked the growth of nerve fibers *ex vivo* for up to 4 weeks.[1] The ability to maintain live tissue outside the body eventually led to the development of immortalized cancerous and noncancerous cell lines, which can grow on plastic dishes treated for cell adhesion and exhibit consistent cell proliferation. The use of these cell lines has become the backbone of life science research with applications ranging from the screening of synthetic and natural products as anticancer agents, mass production of antibodies for therapeutics, and fundamental experimentation to better understand cellular mechanisms and signaling pathways.[2−5] These cultures are attractive for their simplicity, ease of use, reproducibility, and low cost.[6] However, despite their substantial contribution as fundamental research models, cells grown on 2D plastic substrates not only fail to mimic the specific organization and architecture present *in vivo*, but they also show altered morphology, gene expression, and metabolic functions.[7−9] This inconsistency between the *in vitro* and *in vivo* models partially accounts for the high failure rate of pharmaceuticals in the clinical testing stage, where the antidisease agents that show promising response in 2D cell cultures are directly applied to complex animal and human models.[10]

Three-dimensional cell cultures bridge the gap between traditional flat cultures and animal models. While many types of 3D cell culture models exist, we have used spheroids for this work. Cultivated *ex vivo*, spheroids are formed from 2D cell cultures and mimic several key components of live tissue and tumors such as cell−cell and cell-extracellular matrix interactions, nutrient and O_2 gradients, and cellular heterogeneity.[11,12] Due to the close cell packing in these models, a decreasing concentration of nutrients and oxygen penetrating through the spheroid core as well as a reverse gradient of

Received: December 19, 2024
Revised: January 15, 2025
Accepted: January 17, 2025
Published: March 10, 2025

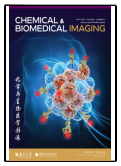

metabolic waste moving outward from the center of the model can be observed.[13] These concentration differentials result in the formation of three distinct microenvironments in large spheroids (*diameter >400 μm*). The outermost layer, the proliferation zone, is composed of rapidly dividing cells.[14] The second layer is inhabited by cells in a dormant, nonproliferative state and is called the quiescent zone.[15] The innermost layer is the necrotic core, distinguished by its hypoxic environment and the buildup of metabolic waste. This layer displays an acidic pH and elevated levels of reactive oxygen species (ROS).[16] These elevated ROS levels, in conjunction with the Warburg effect in malignant tumor models, have previously been implicated in chemotherapy and radiation resistance.[17]

Though promising, 3D cell culture technology is still in its infancy. Spheroids have mainly been characterized using imaging techniques such as fluorescence microscopy, confocal microscopy, two-photon microscopy, and fluorescence lifetime imaging microscopy.[18−21] These techniques have allowed for the elucidation of drug transport into the spheroid as well as the internal structural organization of the spheroid.[22] Additionally, mass spectrometry has recently emerged as a powerful tool for spatially resolved proteomic and metabolomic analysis of spheroids.[23] Techniques such as matrix-assisted laser desorption/ionization mass spectrometry imaging and desorption electrospray ionization mass spectrometry have previously been explored for their ability to analyze the metabolic heterogeneity in spheroids.[24] While great for benchmarking, these techniques have substantial drawbacks. For example, fluorescence microscopy techniques have previously been brought under question for significantly altering conditions in the probed system due to phototoxicity induced by the fluorescent tags employeed.[25,26] Additionally, a major challenge with mass spectrometric analysis stems from the heterogeneous distribution of metabolites and proteins in the spheroid as it grows.[27] This spatial variability complicates the interpretation of mass spectrometry findings, as the analysis may not accurately represent the spheroid's overall composition.[28] Furthermore, both techniques require extensive sample prep and are often unable to track the live production of reactive oxygen species in 3D cultures.[24,29] Thus, there remains a need for analytical tools capable of real-time analysis of biological processes in spheroids.

Electrochemistry has recently been used to study 3D cell cultures as it allows for real-time, sensitive, and selective quantification of metabolites. For example, Utagawa et al. recently developed a porous membrane sensor capable of *in situ* glucose measurements in breast cancer spheroids.[30] Additionally, the Shiku group used electrochemiluminescence to analyze excreted signaling molecules from spheroids.[31] Using a luminol analog system, they measured the hindrance at the electrode surface caused by molecules excreted from the spheroid as a function of time and potential. In our study, we aim to build upon a similar electrochemiluminescence system and use it to characterize H_2O_2 concentrations in spheroids. H_2O_2 is a key indicator of cell health with elevated peroxide levels capable of triggering cell apoptosis. Additionally, H_2O_2 has a lifetime measurable in seconds to minutes as opposed to other radical species such as hydroxyl radicals or superoxide anions which have lifetimes of nanoseconds and microseconds, respectively.

Electrochemiluminescence (ECL) is an excited state electrochemical technique in which redox reactions cause an excited state to be formed in a luminophore, thus, leading to the emission of photons.[32] There are two special characteristics of ECL: 1. the noise of the experiment is dictated by the detector since there are no excitation photons, unlike fluorescence, and 2. the emission layer is governed by the very short radical lifetimes formed in these reduction−oxidation reactions. Briefly, coreactant ECL occurs when the co-oxidation or coreduction of a luminophore and sacrificial coreactant takes place. The newly formed oxidized or reduced coreactant forms a radical, which can then undergo a homogeneous charge-transfer with the oxidized or reduced luminophore to form the excited state, which may radiatively emit a photon.[33]

Recently, the rise of ECL microscopy has been shown in many contexts. There are two main types of ECL microscopy: light mode and dark mode ECL microscopy. In "light" mode the luminophore is tagged onto the entity to produce photons at the surface. However, in dark mode, also known as *"shadow"* mode, the luminophores are solvated in solution to produce a negative image of the object.[34] We will be utilizing shadow ECL microscopy throughout this paper. ECL microscopy has been used to inform on single mitochondria,[34] extracellular matrix,[35] multiphase systems,[36−40] mammalian cell morphology,[41,42] and the electro-precipitation of radical salts,[43] among others.[44,45] Overall, it has shown to be an incredibly powerful analytical tool with unprecedented spatial resolution at the surface of a conductive interface.[46]

When comparing ECL microscopy to fluorescence microscopy (the technique of choice for spheroid analysis) it is important to consider the analytical figures of merit of the two. ECL offers several advantages over traditional fluorescence methods. For instance, ECL systems can achieve lower background noise and higher sensitivity due to the controlled nature of the electrochemical reaction, which allows for the precise tuning of the reaction conditions without the need for excitation photons.[47,48] Additionally, this technique is "label-free" thus providing spatial information regarding the chemical distribution of analytes without the need for antibodies tags or other molecules. For example, in imaging single mitochondria, ECL provided superior spatial resolution, imaging down to 500 nm, without the inclusion of dye.[34] Furthermore, when examining morphologies of cells, processes such as autofluorescence can be detrimental to spatial resolution. With ECL, this challenge is eliminated; and has been experimentally shown to have increased spatial resolution for cell−cell junctions, and spindle-like structures.[49]

While there are many different luminophores to choose from, we selected luminol due to its reaction with the hydrogen peroxide coreactant.[50,51] Herein, we first establish the viability of luminol electrochemiluminescence as a diagnostic tool for the quantification of hydrogen peroxide in spheroids as they mature using noncancerous mammalian human embryonic kidney (HEK 293) spheroids. With this spheroid system, we see that H_2O_2 concentrations can be significantly identified as soon as 3 days after spheroid seeding, signaling the beginning of necrotic core formation. Subsequently, we use this technique to quantify H_2O_2 produced in response to stress induced by the drug irinotecan in noncancerous spheroids. We show that as drug concentration increases, ECL intensity increases in response to the upregulation of H_2O_2 concentrations in the proliferation layer of the spheroid. After demonstrating the technique's ability to monitor drug-induced responses in noncancerous cell lines, we apply the luminol-ECL system to investigate the Warburg effect on MCF-7 and MDA-MB-231 breast cancer

https://doi.org/10.1021/cbmi.4c00105
Chem. Biomed. Imaging 2025, 3, 310−321

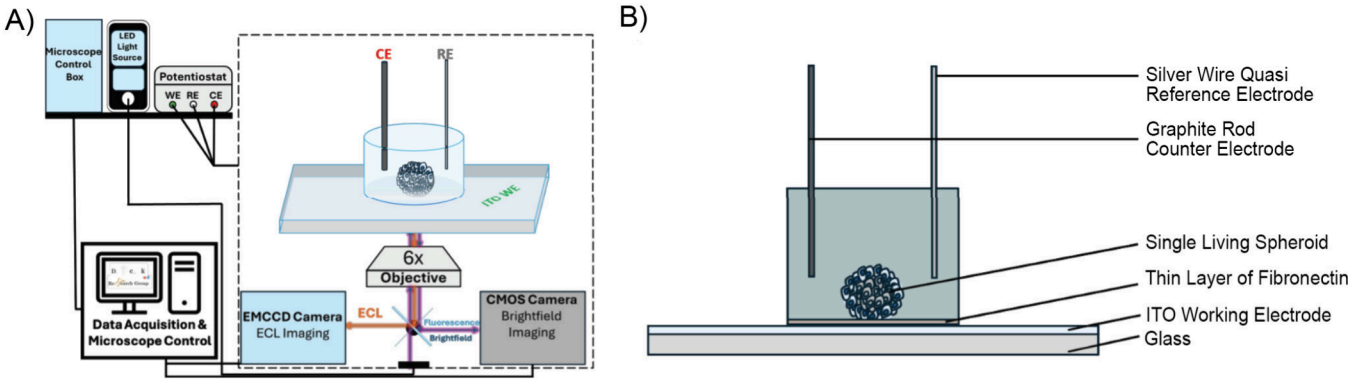

Figure 1. A) Electrochemiluminescence microscopy experimental setup used to obtain micrographs. Electrochemistry is controlled by a CH Instruments Potentiostat. Imaging was performed with a Hamamatsu Orca CMOS camera for brightfield and fluorescence imaging, while an Andor iXon EMCCD camera acquired ECL micrographs. A 4× objective, with a 1.5× modifier, was used to acquire images. **B)** ITO-glass cell constructed in-house with an ITO working electrode, a silver wire quasi reference, and a glassy carbon rod as the counter electrode. The selected spheroid was immobilized on the surface of the ITO using a thin layer of fibronectin. Objects are depicted for clarity, not for scale.

spheroids by altering endogenous H_2O_2 production using metabolic drugs rotenone, and carbonyl cyanide-p-trifluoromethoxyphenylhydrazone.

MATERIALS AND METHODS

Materials and Reagents

All reagents were used *"as received"* without further purification steps. The reagents used were DPBS (1X) (Gibco Co.), Luminol (≥97%, Sigma-Aldrich Co.), 30% Hydrogen Peroxide (Fisher Chemical), Glucose (ThermoFisher Scientific), Irinotecan (ThermoFisher Scientific), FCCP (ThermoFisher Scientific, 10 mM suspended in DMSO), Fibronectin (Sterile Filter Bovine Plasma Filtered, ThermoFisher Scientific) and Rotenone (ThermoFisher Scientific). Twenty-five mM of Glucose was added to the 1X DPBS and held overnight at 4 °C. In all trials, 5 mM of pH 8 luminol was suspended in the glucose-DPBS. The hydrogen peroxide-luminol calibration curve was generated using serial dilutions from the 30% hydrogen peroxide stock in the presence of 5 mM luminol in glucose-DPBS. The data presented in Figure 2 used 100 mM of hydrogen peroxide with 5 mM luminol in the glucose-DPBS solution.

ITO Electrochemical Cell Fabrication

The indium tin oxide (ITO) working electrode (Huany Co., China) was laser cut into pieces of 25 mm × 25 mm approximate dimensions. Then the ITO electrodes were epoxied onto a glass tube (r = 19 mm, h = 20 mm) and a small piece of copper tape was used to connect the ITO layer to an alligator clip to the potentiostat. Fibronectin was used to immobilize spheroids onto the ITO electrodes.

Optical Microscopy and Electrochemistry

A Nikon Eclipse Ti2 inverted optical microscope (Nikon, Japan) was used to conduct microscopy experiments. The light source equipped is a D-LEDi light source (Nikon, Japan) and was used for fluorescence imaging. Brightfield was conducted with an external MKII (Nikon, Japan) light source. The objective used was 4× with a numerical aperture of 0.20 and a working distance of 20 mm. The internal 1.5× modifier was used in all experiments for a total of 6× magnification. An EMCCD iXon 888 camera (Andor Technology Ltd., Belfast, UK) was used with a 116 ms exposure time. The exposure time of 116 ms was chosen for these ECL microscopy experiments to balance both the spatial and temporal resolution requirements of these experiments. This exposure time allows for an adequately high spatial resolution needed for the accurate measurement of the low-intensity ECL signal for low H_2O_2 concentrations while also enabling a fast temporal resolution that is required to map the mass transfer-limited ECL signal. The 116 ms exposure time is shorter, and therefore the frame rate is faster, at about 3 fps, than conventional ECL microscopy experiments that routinely used exposure times ranging from 250 ms to 5 s so that the high temporal resolution was achieved in these experiments. The parameters of a 10 MHz quality mode, 4.22 μs shift speed, and temperature of −75 °C were also used. The other equipped camera was a Complementary Metal-Oxide Semiconductor (CMOS) camera from Hamamatsu (Orca-Quest qC-MOS C15550−20UP, Hamamatsu, Japan). All images were acquired through the NIS Elements Software (Nikon, Japan).

At the inverted optical microscope, an electrochemical cell was placed on the stage. In these experiments, an Indium Tin Oxide (ITO) (Huany Co., China), working electrode is used. The counter electrode used was a glassy carbon rod (CH Instruments, Austin, TX), and the quasi-reference electrode was composed of an Ag rod (CH Instruments, Austin, TX). A schematic of the different 3-electrode experimental setup can be found in Figure 1A. The potentiostat used was a CH Instruments 601E (CH Instruments, Austin, TX).

Cyclic voltammetry was used for the ECL reaction. The parameters are initial E = 0.1 V, high E = 1.8 V, low E = 0.1 V, initial scan direction = positive, scan rate = 100 mV/s, sweep segments = 2, sample interval = 0.001 s, quiet time = 5 s, and sensitivity = 0.01. The frame with the highest mean intensity through the spheroid was analyzed.

Cell Culture and Spheroid Synthesis

Human embryonic kidney cells (HEK293, ATCC number CRL-1573), breast cancer cells (MCF7, ATCC number HTB-22), and triple negative breast cancer cells (MDA-MB-231, ATCC number HTB-26) were cultured in Dulbecco's Modified Eagle's Medium with high glucose (Sigma-Aldrich, D6429−500 ML) supplemented with 10% Fetal Bovine Serum (VWR, 97068−085) 1.5% Penicillin−Streptomycin (Sigma-Aldrich, P0781−100 ML) until they reached 90% confluence. At this time, cells were lifted using TrypLE Express Enzyme (1X) (Thermofisher Scientific, 12605010) and plated in ultralow attachment, rounded bottom 96 well plate (Corning, 7007) with a concentration of 2×10^4 cells per well for each cell line. The cells were allowed to grow for a maximum of 9 days before analysis with a 75% media change every other day at 37 °C and 5% CO_2.

Irinotecan Toxicity Study

To evaluate the impact of the chemotherapeutic irinotecan on HEK 293 spheroids, the appropriate amount of the drug was dissolved in DMSO to make a 1 mM irintecan solution. This solution was then diluted using cell culture PBS to varying concentrations in a 96 well plate. Spheroids were incubated for 24 h in the drug-media solution and rinsed with new media before adhesion to the fibronectin layer in the ITO glass cells for analysis.

For the fluorescence analysis, spheroids were incubated at the respective times, rinsed with media, and incubated with Calcien AM live fluorescent stain and hoechst nuclear fluorescent stain for 30 min.

https://doi.org/10.1021/cbmi.4c00105
Chem. Biomed. Imaging 2025, 3, 310−321

At this time, the media was replaced again, and the spheroids were imaged at an inverted fluorescent microscope.

Rotenone and FCCP Study

Metabolic drug studies were conducted on MCF7 and MDA-MB-231 spheroids. Rotenone was prepared by dissolving the appropriate concentration of the drug in DMSO to obtain a 2 mM stock solution. This stock was then diluted to 2 μM concentration with the luminol analysis solution and placed in the ITO glass cells containing the spheroid. The spheroid was then incubated for 15 min before the ECL analysis. Carbonyl cyanide-p-trifluoromethoxyphenylhydrazon (FCCP) was obtained as a 2 mM stock solution containing DMSO. It was also diluted to 2 μM concentration with the luminol analysis solution and placed in the ITO glass cells containing the spheroid. The spheroid was then incubated 15 min before the ECL analysis.

RESULTS AND DISCUSSION

Microscopy Correlated Electrochemiluminescence for the Illumination of Spheroids

Electrochemiluminescence can be combined with optical microscopy to visualize 3D cell culture models such as spheroids. A schematic of the setup is shown in Figure 1A. Briefly, an electrochemical cell was fabricated using an optically-transparent indium tin oxide (ITO) working electrode upon which a glass cylinder was epoxied to hold the ECL solution, silver wire quasi-reference electrode, and a graphite rod counter electrode. The three-electrode cell was placed on top of an inverted microscope functionalized with a CMOS camera to acquire brightfield and fluorescence micrographs, and an EMCCD camera to conduct the ECL imaging. A 4× long working distance was used with a 1.5× modifier internal to the inverted optical microscope. The electrochemistry was controlled via a commercially available potentiostat and the data acquisition, along with microscope control, was conducted on a computer.

In a standard experiment, the homemade ITO-glass cell was modified using a thin layer of fibronectin, a high-molecular-weight glycoprotein found in the extracellular matrix (ECM) and blood plasma. Postmodification, the fibronectin layer facilitated the immobilization of the spheroid onto the ITO-glass cell for facile experimentation (Figure 1B). This layer allowed for expedited solution changes during experimentation and it did not significantly alter the signal obtained during the measurement, though a ∼0.1 V shift in the oxidation potential of luminol was observed (Figure S1). This shift, likely due to the fibronectin layer, falls within the range reported in the literature and does not impede the ECL reactions[52] (Figure S1). After immobilization of the spheroid, the ITO cell was positioned on the microscope, and the focal plane was manipulated such that the edges of the spheroids were in direct focus. This focusing strategy eliminated any discrepancy in ECL intensity that might arise as a function of differences in spheroid thickness. After focusing, the 5 mM luminol solution was added to the glass cell and potential was cycled to excite the luminol and coreactant to yield the ECL signal.

Visualization of Endogenously Produced H_2O_2 in Kidney Spheroids

Reactive oxygen species (ROS) are a group of highly reactive oxygen-containing molecules, including superoxide anion ($O_2^{\bullet-}$), hydrogen peroxide (H_2O_2), hydroxyl radical ($HO^{\bullet}$), and singlet oxygen.[53] In the context of biological applications, this term is often stretched to include reactive nitrogen, sulfur, carbon, selenium, and halogen (RHS) species.[44] These species can participate in oxidation−reduction reactions, leading to oxidative modifications of biological macromolecules, which in turn contribute to redox signaling and overall biological function.[45] While it has previously been noted that these species nonspecifically interact with proteins, lipids, nucleic acids, and carbohydrates to generate toxic byproducts in cell cultures, H_2O_2 has been implicated in influencing cellular behavior, including invasion, proliferation, and apoptosis in spheroids and tumor models.[54] Specifically, this molecule plays a crucial role in regulating cellular behavior. H_2O_2 is produced at low levels during cellular respiration in all cells, but higher concentrations have been shown to induce oxidative stress leading to cell death.[55] For instance, H_2O_2 concentrations above 0.05 mM can trigger cell death through ROS accumulation, while lower concentrations activate protective mechanisms to preserve redox balance.[46] This dual effect highlights the significance of characterizing the behavior of this small molecule in models aiming to mimic tissues or tumors *in vivo*.

It has previously been shown that the use of luminol-based electrochemiluminescence allows for the sensitive targeting of H_2O_2 as light is emitted by the luminol radicals when they combine with hydrogen peroxide radicals. To investigate if it is possible to visualize the H_2O_2 produced by spheroids, human embryonic kidney (HEK 293) spheroids were tested in H_2O_2 only, in luminol only, and in a solution of luminol and H_2O_2 (Figure 2). HEK 293 cells were first grown in 2D culture format and then plated in ultralow attachment well plates to form spheroids. The initial cultivation of cells in 2D cell culture format allowed for the easy assessment of cell growth, morphology, and proliferation rates, as well as to obtain the optimal cell density of 1×10^6 cells per plate from which 1×10^5 we plated in each well of a 96 well plate to form spheroids. These spheroids were allowed to mature for 9 days until three distinct layers could be visualized in the spheroids using optical

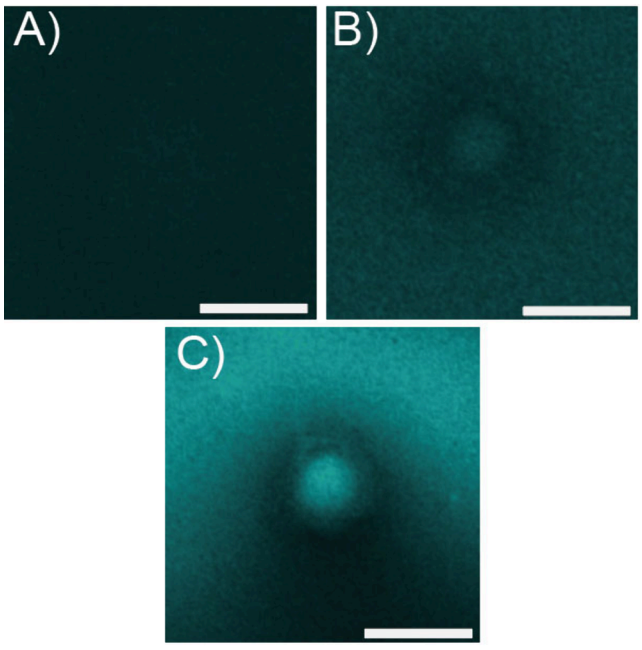

Figure 2. Control experiments taken on ITO-glass cells with **A)** H_2O_2 only, **B)** luminol only, and **C)** luminol and H_2O_2 to allow for the benchmarking of the luminol-H_2O_2 system using microscopy. Scale bar = 500 μm.

https://doi.org/10.1021/cbmi.4c00105
Chem. Biomed. Imaging 2025, 3, 310−321

microscopy, and then ECL analysis was performed. Stemming from transformed kidney cells, these spheroids were non-cancerous and chosen for their reproducible growth and well-characterized behavior.[56] As a negative control, spheroids were placed in 0.1 mM H_2O_2, and voltage cycled using cyclic voltammetry from 0.1 V vs Ag/AgCl to 1.8 V vs Ag/AgCl. The resulting electrochemiluminescence was recorded (Figure S1). Upon current application, a nonzero starting current was observed. This can be attributed to the fibronectin layer applied on the ITO surface to immobilize the spheroid onto the electrode. As discussed previously, fibronectin consists of high-molecular-weight glycoproteins that can adhere to the ITO surface, partially passivating it and influencing its electrochemical properties. As the formation of H_2O_2 radicals does not result in photoemission, no ECL was observed (Figure 2A). As a positive control, spheroids were immersed in a solution of 5 mM luminol along with 0.1 mM H_2O_2, and a potential was applied as before. Luminol reacts with radicals produced by peroxide, generating an excited form of 3-aminophthalate that emits photons,[57] and enabling the visualization of the spheroid in solution (Figure 2C). Given that the hydrogen peroxide was added exogenously, an increased light intensity was expected around the spheroid as can be seen in the micrograph. Interestingly, we were able to visualize high ECL intensities in the center of the spheroid as well. As ECL should only occur in the presence of both luminol and hydrogen peroxide, we hypothesized that either peroxide was quick to diffuse into the spheroid and concentrate there, resulting in a brighter emission due to increased concentration, or it could be a combined effect where the core of the spheroid might produce its own supply of H_2O_2 along with that diffusing in, resulting in a higher signal. If it was the former case, removing peroxide should eliminate the ECL signal in the center of the spheroid. However, if it was the latter and the spheroid produced its own supply of H_2O_2, ECL should persist regardless of peroxide addition into the system.

To test this, H_2O_2 was removed from the system and a new spheroid sample was interrogated with only 5 mM luminol. Upon voltage application, ECL was observed again with the center of the spheroid showing a higher intensity of light compared to the spheroid edges and the bulk solution (Figure 2B). This supported the hypothesis that the spheroid core itself can produce hydrogen peroxide which can then react with the luminol to yield ECL. This observation is consistent with previous reports of increased ROS activity in mature spheroids as a function of hypoxia, core acidification, and necrosis.[58]

In our experiment, it is important to note that ECL is fundamentally a surface characterization technique, as it relies on the generation of light through electrochemical reactions occurring at the electrode surface.[59] This applies to two crucial aspects of our work. The first one is that due to this technique's ability to show electrochemical reactions at the electrode solution interface, any heterogeneity in spheroid curvature and geometry that alters the electrode-spheroid contact can result in variation in ECL intensity. For example, cell surfaces closer to the electrode might generate more ECL compared to those further away because the diffusion distance that the luminol intermediates must travel is shorter. It is important to note that the spherical geometry of the spheroid creates a distance between the electrode and its outer edges, which may prevent luminol intermediates from efficiently traveling to the outer regions where the reaction with endogenous H_2O_2 is less likely to occur. As a result, the central region of the spheroid, being closer to the electrode, produces a stronger ECL signal, while the edges exhibit less intensity. This limitation arises from the diffusion dynamics of H_2O_2 and the spatial configuration of the spheroid, which affects the overall distribution of the ECL signal. In this study, this problem was mitigated by standardizing spheroid growth procedures to yield consistently sized spheroids that looked optically similar under brightfield microscopy. Additionally, the 3D cell structures were attached to the electrode with fibronectin. Each electrode was incubated with the same amount of fibronectin solution which ensured homogeneous surface coverage.

The second aspect is that the technique only reports on molecules that can successfully diffuse to the electrode surface. Although the vertical resolution is determined by the depth of field, it is not likely that the brightness observed at the center of the image is due to the reaction occurring at the spheroid core, which is 100s of microns away from the electrode.[41] Instead, our technique reports on the hydrogen peroxide formed in the core that can diffuse to the outer reaches of the tissue closer to the electrode surface. As the production of peroxide in the core increases, higher ECL intensities should be observed in the spheroid center on the micrograph as more hydrogen peroxide is available to diffuse to the outer tissue. The concentration of H_2O_2 in the tissue closest to the electrode can be approximated using a calibration curve generated through the interrogation of luminol solutions containing different concentrations of H_2O_2. Note that the calibration curve exhibited two distinct linear regions, with greater sensitivity observed at lower hydrogen peroxide concentrations. However, a single calibration curve was used because literature values for hydrogen peroxide in spheroids typically range between 50 and 80 μM, which falls within the linear region of the calibration plot. The detection limit obtained from this curve was 2.26 ± 0.58 μM (Figure S2). This limit of detection was determined by using the camera's average noise and standard deviation. The noise was multiplied by 3 and summed with the average to find the limit of detection in signal units (Figure S2). It is important to consider here that luminol is soluble only in basic conditions and, thus, our reaction solution has a pH of 8. To ensure that this deviation from physiological conditions has minimal impact on our results, the amount of time the spheroids spent in the luminol solution was minimized. Moreover, a cell viability assay was conducted to confirm spheroid viability in the luminol solution after an hour of incubation at 37 °C, a time point that far exceeds the analysis window for our system (Figure S3). Overall, we have demonstrated a novel technique to visualize endogenously produced hydrogen peroxide in HEK 293 spheroids.

We also find it pertinent to mention the analytical figures of merit for shadow electrochemiluminescence here for clarity. Specifically, the "background" (the spatial area surrounding the spheroid) is not a true background in the figure, due to it being a negative image, and is dependent on the distribution of the coreactant and luminophore molecules in solution. Since we are not in light ECL (also known as positive ECL) mode the luminophore is not spatially confined to the entity (spheroid) thus can diffuse into solution. Thus, we are allowing the luminol to permeate into the spheroid. Additionally due to the high temporal resolution (*ca.* 30 frames per second) to map

https://doi.org/10.1021/cbmi.4c00105
Chem. Biomed. Imaging 2025, 3, 310−321

the mass transfer-limited ECL signal accurately, low signal is expected and resolved. However, due to the sensitivity of the cold (−70 °C) EMCCD camera, this still allows us to extract statistically significant data when the region of interest is selected within the spheroid, *infra vide* (Figure 3).

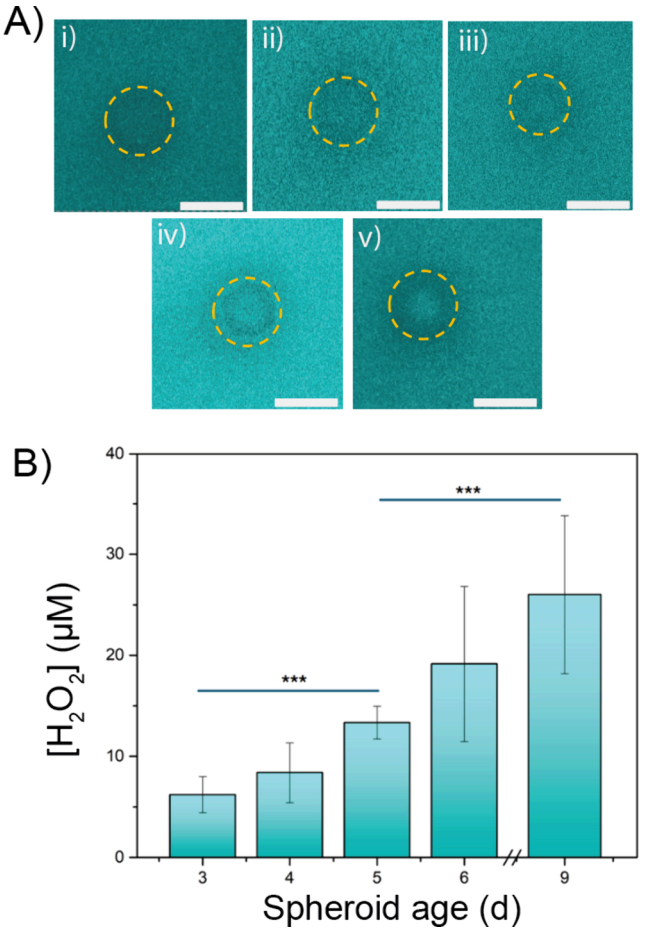

Figure 3. A) Electrochemiluminescence images taken at (i) 3 days, (ii) 4 days, (iii) 5 days, (iv) 6 days, and (v) 9 days after spheroid seeding. **B)** Extrapolated H_2O_2 concentrations in the spheroid core at different time points using calibration curve showing significant difference between spheroids at day 5 through 9 when compared to day 3 but no difference between day 3 and day 4. Scale bar = 500 μm and error obtained from the average of the three highest intensity points in the spheroid.

Quantification of Hydrogen Peroxide Production with Increasing Spheroid Age

During the early stages of spheroid formation, as cells proliferate and aggregate, they undergo metabolic shifts that can lead to increased production of reactive oxygen species (ROS), including H_2O_2. Wartenberg et al. showed that the size of tumor spheroids correlates with ROS levels, with smaller spheroids—composed mainly of proliferative cells—exhibiting lower ROS levels compared to larger, slower growing spheroids, which are chemotherapy and radiation resistance.[60] This indicates that H_2O_2 production may begin soon after spheroid formation as cells adjust to their new 3D environment. To investigate this phenomenon using our system, HEK 293 spheroids were formed as before and interrogated using ECL on different days postseeding. After being transferred from 2D cell cultures, it takes approximately 24 to 48 h (about 2 days) for the establishment of cadherin-mediated adhesions that bind the cells together into a sphere-like conformation.[61] Thus, we started the spheroid maturity study on day three after seeding. In addition, ECL images were obtained on day 4, day 5, day 6, and day 9. Figure 3A shows the microscopy images obtained and highlights the perimeter of the spheroid. Comparing the samples, we see an even distribution of light intensity inside the perimeter of the spheroid at day 3 and 4. Qualitatively, at day 5, intensity in the center is only marginally higher, while at day 6, a clear intensity difference can be observed between the perimeter and the center of the spheroid. On day 9, the center was considerably brighter, suggesting that there was a higher concentration of H_2O_2 at the spheroid center. The concentration of hydrogen peroxide in the spheroid was obtained using the calibration curve and the resulting values are shown in Figure 3B as a function of days after seeding. There was no significant difference between the peroxide concentration on days 3 and 4 but our technique could quantify the difference between days 3 and 5 with H_2O_2 concentrations of 6.20 μM and 8.39 μM, respectively. A significant difference was also observed across days 5, 6, and 9 with concentrations of 13.33 μM, 19.14 μM, and 25.99 μM, respectively. The increased hydrogen peroxide concentration suggests that the spheroid begins to undergo a metabolic shift as early as 4 days after formation.

Previous research has quantified the H_2O_2 concentration in the core to be between 50 μM to 80 μM in the core at maturity for colorectal and tongue cancer spheroids.[62,63] This discrepancy between our results and previously reported values comes from the fact that each type of cell line produces differing concentrations of peroxide. Additionally, while the average values in literature come from cancer cells, we are using a noncancerous cell line which is expected to have lower ROS activity as their ROS species are primarily generated as a byproduct of glycolysis and oxidative phosphorylation, while ROS species in cancerous cell lines are primarily produced through aerobic glycolysis.[64,65] To the author's knowledge, our work is the first of its kind where hydrogen peroxide produced by the spheroid core can be quantified in real-time without the need for fluorescent labeling or sample destruction.

Visualization of Irinotecan-Induced ROS Stress in Noncancerous Spheroids

Spheroids have been widely utilized to study the mechanisms of drug action for new pharmaceutical agents such as irinotecan. Irinotecan is a camptothecin analogue used as a chemotherapeutic agent to treat various cancers such as colorectal cancer and other solid tumors.[66] This drug is hydrolyzed by carboxylesterases to form its highly active metabolite in actively respirating cells which exerts its cytotoxic effects by inhibiting the activity of DNA topoisomerase I.[67,68] In addition, irinotecan activates NADPH oxidases that catalyze the production of superoxide that is converted to H_2O_2, thus increasing ROS activity. Taking this mechanism into account, we wanted to see if our ECL technique could report on changes in H_2O_2 concentration as a function of irinotecan exposure. To investigate this phenomenon, mature spheroids were incubated in 0 μM, 0.5 μM, 5 μM, 25 μM, and 50 μM for 24 h. Postincubation, spheroids were washed using phosphate buffered saline and attached onto fibronectin coated ITO cells before the electrochemical measurements. Figure 4A shows the brightfield images of the spheroid in the first row, followed by the fluorescence emitted by luminol in the spheroids, and

https://doi.org/10.1021/cbmi.4c00105
Chem. Biomed. Imaging 2025, 3, 310−321

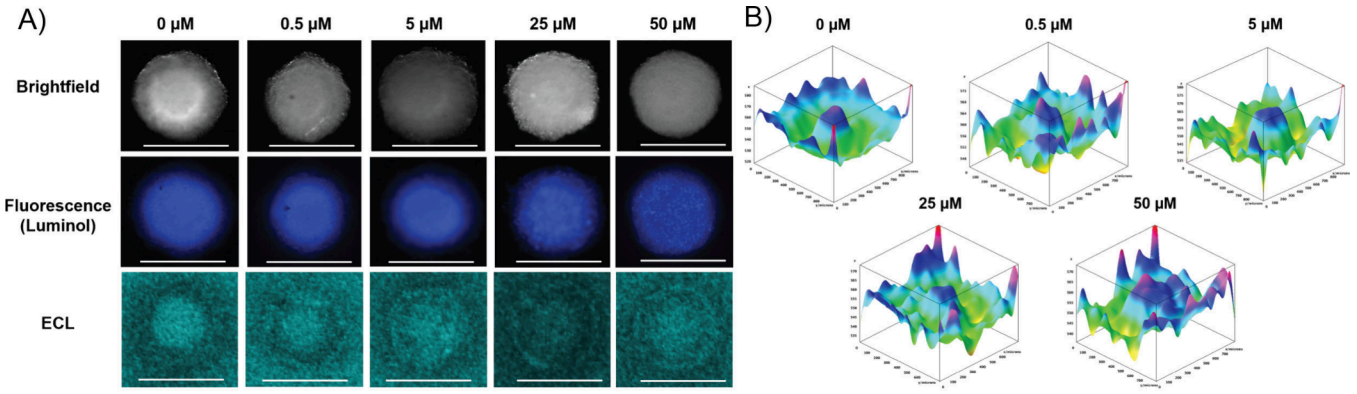

Figure 4. Tracking H_2O_2 production as a function of irinotecan-induced ROS stress. **A)** Comparative microscopy images obtained after incubating spheroids in varying concentrations of irinotecan to show brightfield view, luminol fluorescence, and electrochemiluminescence. **B)** Surface intensity plots highlight the distribution of ECL intensity across different concentrations of irinotecan. Scale bar = 500 μm.

finally the ECL trace. The brightfield images in the first row show consistent spheroid diameters of approximately 500 μm at all concentrations of irinotecan indicating that the overall morphology of the cell culture does not change as a function of drug administration. Additionally, the fluorescence traces revealed a uniform distribution of luminol across the spheroid, with no bias toward the center or the periphery. In line with previous findings, the ECL traces at all concentrations exhibited greater intensity at the spheroid's center, reflecting higher H_2O_2 levels in this region. However, while the central intensity remained stable, increasing irinotecan concentrations led to enhanced ECL intensity at the spheroid edges with 50 μM showing the change most distinctly (Figure 4A).

To better visualize this phenomenon across the surface of the spheroid, three-dimensional surface intensity plots were obtained with the x- and *y*-axis reporting the distance from one end of the spheroid and the *z*-axis reporting the ECL intensity (Figure 4B). The 0 μM control sample showed the highest intensity at the center of the surface plot as evidenced by the distinct purple peak followed immediately by the green/yellow valley. This topographical profile is consistent with previous observations that the center of a mature spheroid is nutrient-deprived and hypoxic with increased ROS activity, while the periphery is composed of proliferating cells that show lower ROS activity.[69] Similar results were seen for 0.5 μM and 5 μM irinotecan concentrations where a clear central peak is observed surrounded by low-intensity valleys representative of the spheroid edges. However, as drug concentration increased to 25 μM and 50 μM, higher intensity peaks are seen throughout the surface of the spheroid in addition to the center, with the effect being most pronounced for the 50 μM sample where nearly the whole spheroid surface displayed elevated ECL intensities. Recall that higher ECL intensity in the luminol-H_2O_2 system corresponds to upregulated levels of H_2O_2, and irinotecan has previously been shown to increase H_2O_2 production.[42] Thus, our observations imply that irinotecan is most successful in inducing H_2O_2 production in the proliferation zone of the spheroid as the intensity at the center of the spheroid remains consistent across all samples while the intensity at the periphery of the spheroid increases with increasing irinotecan concentration. The preferential increase is most likely due to the drug's inability to diffuse into the densely packed spheroid. Drug diffusion limitations are a common issue for many pharmaceuticals agents, which limit their efficacy when faced with solid tumors in the human body. Our technique's ability to spatially resolve H_2O_2 production as a function of drug distribution can be extended to other pharmaceutical reagents that are known to function via ROS generation mechanisms and could potentially be used as a diagnostic tool to visualize the upregulation of H_2O_2 production as a side effect of the Warburg effect.

Visualization of the Warburg Effect Using Electrochemiluminescence

First described by Otto Warburg in the 1920s, the Warburg effect refers to the tendency of cancer cells to favor glycolysis for energy generation, even when oxygen is readily available, resulting in elevated glucose consumption and lactate formation.[70] In noncancerous cells, glucose is first broken down into pyruvate through glycolysis in an anaerobic process and then transported to the mitochondria where it is oxidized through the Krebs cycle and moved through the electron transport chain to generate ATP in an aerobic reaction.[71] In the absence of oxygen, pyruvate is converted to lactic acid resulting in a reduced yield of ATP.[61] Of the two processes, the mitochondrial reactions, also known collectively as oxidative phosphorylation, are preferred as they yield more ATP.[61] Unlike noncancerous cells, tumor cells prefer the lactic acid pathway even in the presence of oxygen, likely due to the ability of lactic acid to influence various signaling pathways that can promote tumor progression and metastasis.[72]

The Warburg effect is a hallmark of malignant tumors and has been previously demonstrated in cancer cell-derived spheroids.[73] These spheroids exhibit the cellular heterogeneity mentioned earlier, with the Warburg effect being most pronounced in the core of the spheroid due to the hypoxic environment, which favors the lactic acid cycle. The increased lactic acid production also results in accelerated production of H_2O_2 and other ROS species, which are byproducts of aerobic glycolysis.[62] We can harness this increased peroxide production to visualize the Warburg effect in cancer spheroids using ECL. To demonstrate this, we cultured MCF-7 estrogen positive and MDA-MB-231 triple negative breast cancer spheroids. Both cell lines were first grown in 2D culture format and then plated in ultralow attachment well plates to form spheroids. The spheroids were allowed to mature for 9 days until three distinct zones could be visualized in the spheroids using optical microscopy, and then ECL analysis was performed. As observed by other groups, MDA-MB-231 do not form compact, circular spheroids like HEK 293 and MCF-7 spheroids which can be attributed to their spindle-like

https://doi.org/10.1021/cbmi.4c00105
Chem. Biomed. Imaging 2025, 3, 310−321

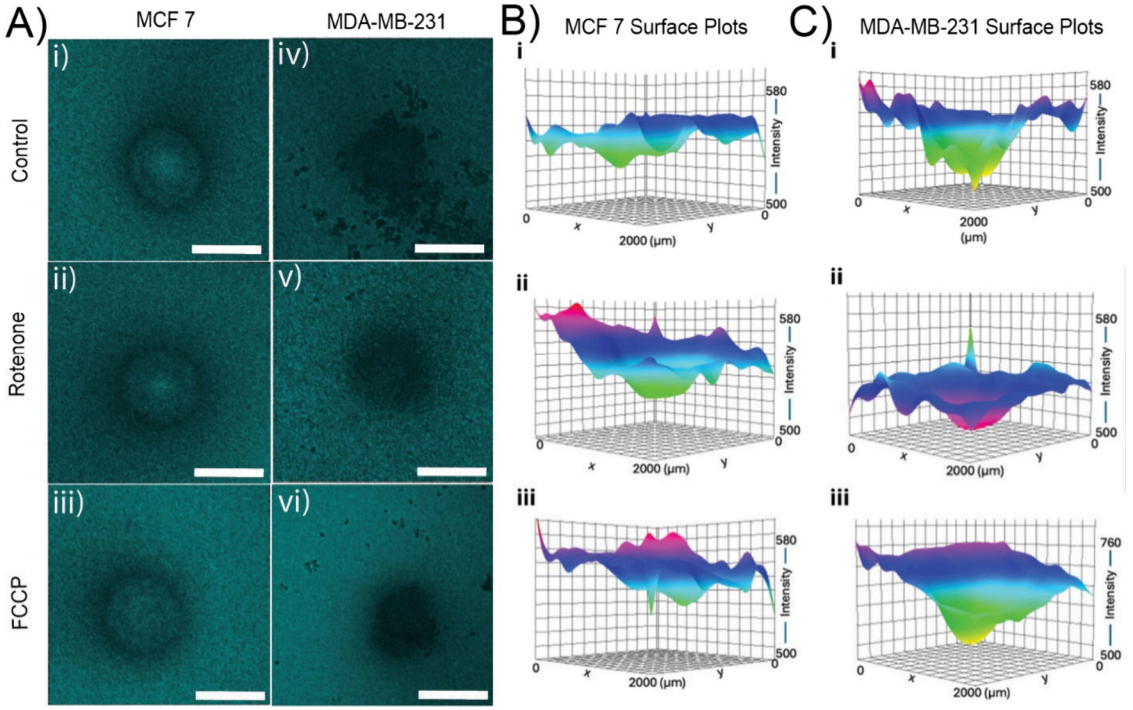

Figure 5. Characterization of MCF-7 and MDA-MB-231 spheroids using ECL. **A)** ECL micrographs of MCF7 and MDA spheroids. Controls (without the addition of metabolic regulators) are depicted in (i) and (iv). ECL micrographs for MCF7 and MDA spheroids incubated with Rotenone are given in (ii) And (v). ECL micrographs for MCF7 and MDA spheroids incubated with FCCP are given in (iii) And (vi). **B)** Surface intensity plots for MCF7 (i) spheroid control, (ii) incubated with Rotenone, and (iii) incubated with FCCP. **C)** Surface intensity plots for MDA spheroids (iv) control, (v) incubated with Rotenone, and (vi) incubated with FCCP.

morphology in 2D cell culture as opposed to the basal-like morphology of the other two cell lines.[74] This loosely connected morphology allows the triple negative breast cancer cells to migrate to different tissue and cause metastasis.[64] We chose to use both cell lines to compare the hydrogen peroxide signal across spheroids with different morphologies. Figure 5A(i) and Figure 5A(iv) show the ECL micrographs obtained using MCF-7 and MDA-MB-231 spheroids, respectively. As seen in the figure, the former spheroid type adopted a spherical, compact morphology, while the latter was much more spread out with unattached cells that were once part of the spheroid, littering the ITO-glass cell. To emphasize the ECL intensity distribution around the spheroid, the data is plotted as a surface intensity profile in Figure 5B(i) and Figure 5C(i).

In these graphs, the *x*- and *y*-axis show the spatial dimensions while the *z*-axis reports the intensity of the ECL signal observed with the brighter colors and deeper valleys showing higher ECL intensity. The intensity plots show singular deep valleys that are associated with the location of the spheroids. Between the two types of spheroids, MDA-MB-231 spheroids show higher ECL intensity than MCF-7 as evidenced by the brighter and deeper valley in Figure 5C(i) as compared to Figure 5B(i). This would indicate a higher concentration of hydrogen peroxide activity in the spheroid. This aligns with existing literature, as MDA-MB-231 cells heavily depend on aerobic glycolysis for ATP production, a characteristic of their aggressive and invasive phenotype.[75] An active and fast aerobic glycolysis metabolism can generate higher ROS concentrations compared to those observed in MCF-7 cells which, being estrogen receptor-positive, generally show a more balanced metabolic profile. Although they do participate in glycolysis, they rely on oxidative phosphorylation for ATP production, particularly in normoxic conditions.[65] Under hypoxia, MCF-7 cells can shift to glycolysis, but their metabolic flexibility enables them to sustain a more efficient energy production strategy compared to MDA-MB-231 cells and prevents the upregulation of ROS species like H_2O_2.[65] This is demonstrated by the low intensity observed in the surface plots (Figure 5B(i)). Through this experiment, we show that our technique is not only applicable to non-cancerous tissue spheroids, but it can also comment on the behavior of different cancer spheroids in real-time without the need for exogenous labeling methods.

To evaluate the ability of our spheroid ECL system as a potential diagnostic tool for cancer therapeutics, we utilized metabolism altering drugs rotenone and carbonyl cyanide-p-trifluoromethoxyphenylhydrazone (FCCP) to artificially alter the ROS production in both MCF-7 and MDA-MB-231 spheroid. Rotenone is a naturally occurring isoflavonid derived from plants and is capable of inhibiting mitochondrial complex I in cell effectively initiating cell cycle arrest, inducing apoptosis, and upregulating ROS production in cells that primarily utilize oxidative phosphorylation.[76,77] Meanwhile, FCCP is a potent mitochondrial uncoupler that dissipates the mitochondrial membrane potential interrupting the proton gradient across the inner mitochondrial membrane.[78] This leads to a rapid increase in ROS levels which can cause cellular damage, including lipid peroxidation, protein oxidation, and DNA damage.[79] While both metabolic drugs upregulate the production of H_2O_2 and other ROS species in cells, their reaction pathways are different which, we hypothesized, would result in differing ECL profiles in the breast cancer spheroids.

https://doi.org/10.1021/cbmi.4c00105
Chem. Biomed. Imaging 2025, 3, 310−321

To test our hypothesis, we first incubated both spheroid types with 2 μM rotenone for 15 min before running the ECL experiment. Figure 5A(ii) and Figure 5A(v) show the resulting ECL micrographs. As compared to ECL micrographs without drug addition, one can observe a slight reduction in ECL intensity at the spheroid center in MCF-7 spheroids and a substantial reduction in ECL intensity overall for the MDA-MB-231 spheroid to the point that the edges of the spheroids are no longer defined. The surface intensity plots further highlight this difference in that the MCF-7 sample continues to show similar intensities in valley height and coloration as the control while the MDA-MB-231 shows dramatically reduced intensity as evidenced by the physical transposition of the surface plot to lower intensity values as well as a shallower valley surface (Figure 5B(ii) and Figure 5C(ii)). This result was unusual on two accounts; one is that rotenone has previously been shown to increase H_2O_2 concentrations in cancer cells which should have led to the increase in the ECL intensity but, instead, a decrease in intensity was observed. The second interesting discrepancy was the difference between the response of the two cell lines. To address the first observation, one needs to recall that spheroids are composed of three layers, each of which displays a different metabolism. In pH conditions like those in the core, the mitochondrial respiration rate can decrease, resulting in lower production of H_2O_2.[80] Additionally, rotenone has been shown to interact with various signaling enzymes that modulate ROS production, such as NADPH oxidases in low pH environments, leading to decreased ROS production despite its role as a complex I inhibitor.[70] The MDA-MB-231 cell line, which exhibits greater reliance on aerobic glycolysis—a hallmark of the Warburg effect—shows a higher baseline ROS level. FCCP-induced mitochondrial uncoupling further amplifies H_2O_2 production by exacerbating the glycolytic shift, a response less pronounced in MCF-7 cells due to their metabolic flexibility and capacity to utilize oxidative phosphorylation under stress. This metabolic heterogeneity underscores potential therapeutic avenues targeting glycolysis-dominant tumors.

As both types of spheroids used in this study are mature cancer spheroids displaying a heterogeneous population of cells indicative of a pH gradient, it is possible that the rotenone might be activating one of the NADPH pathways, resulting in a decrease in H_2O_2 concentration. One limitation of our technique is that, unlike fluorescence, it cannot be used to identify which pathway is in effect. However, ECL can be used to visually distinguish between spheroids that show a response to a drug and those that do not with high spatial resolution.

To address the second observation that the MCF-7 cells show little to no change while the MDA-MB-231 cells yield a drastic decrease in intensity, it is important to consider the three-dimensional structure of both spheroids. It was mentioned that the MCF-7 cell line produces compact spheroids while the MDA-MB-231 cell line produces flatter spheroids made up of loosely attached cells. As the cell layers increase in density and the spheroid becomes more compacted, diffusion of drugs and other nutrients is greatly diminished while in a flatter spheroid, there is greater diffusion of the drug to the cells allowing for greater drug impact. Similarly, a topographical increase is seen in the surface plot for MDA-MB-231, which showed an overall brighter ECL signal than both the MCF-7 spheroid incubated with FCCP and the MDA-MB-231 control (Figure 5A(iii and vi), Figure 5B(iii), and Figure 5C(iii)).

Unlike the inhibitory effect observed due to rotenone, FCCP shows an increase in ECL signal intensity. Figures 5A(iii) and 5A(vi) both show an overall increase in the ECL intensity but, as before, MCF-7 shows a less pronounced change than the other cell line. In addition to the drug diffusion argument presented earlier, the ability of MCF-7 spheroids to switch between aerobic glycolysis and oxidative phosphorylation makes them more resistant to metabolic drugs such as rotenone and FCCP which alter only the mitochondrial reactions and not glycolysis. Despite this, unlike rotenone, FCCP does illicit a significant response at the MCF-7 spheroid center most likely because of the uncoupling effect of FCCP which allows for increased oxygen consumption without the corresponding ATP production. This would lead to an overload of electrons that react with oxygen to generate H_2O_2 at the core where cells already have an upregulation of ROS due to the presence of an acidic environment resulting in brighter ECL intensity at the spheroid center (Figure 5A(iii)). This is supported by the surface intensity plot which shows topographical increases around the center of the spheroid which are significantly higher than the background intensity as evidenced by pink mountains in the figure as opposed to the valley observed in the control (Figure 5B(iii)). The differential drug responses observed between the cell lines underscore the importance of metabolic profiling in cancer treatment. Drugs targeting specific pathways, such as glycolysis inhibitors for MDA-MB-231-like tumors, could enhance therapeutic efficacy by leveraging their metabolic dependencies. Similarly, a topographical increase is seen in the surface plot for MDA-MB-231 which showed an overall brighter ECL signal than both the MCF-7 spheroid incubated with FCCP and the MDA-MB-231 control (Figure 5C(iii)). This increase is likely due to accelerated diffusion of the drug into the spheroid due to its flat surface and the fact that MDA-MB-231 spheroids show a greater Warburg effect than MCF-7. This means that they already heavily rely on aerobic glycolysis which results in the production of higher concentrations of H_2O_2, and the uncoupling effect of the drug only exasperates the effect resulting in even higher production of H_2O_2 which can be observed using our method. Thus, based on these results, not only can we quantify the H_2O_2 concentration in different cell types, but we can also track the change in these concentrations in response to drug agents like irinotecan, rotenone, and FCCP.

CONCLUSION

Electrochemiluminescence allows for the selective and sensitive quantification of hydrogen peroxide using a luminol-based reaction. In this study, we introduce ECL as a technique to measure endogenously produced hydrogen peroxide in spheroids at real-time scales without labeling or sample destruction. Although limited by the time needed for spheroid preparation, this technique allows for the quantification of endogenous reactive oxygen species in complex biological systems. We demonstrated its ability to track spheroid maturity over time as a function of increasing hydrogen peroxide diffusion from the spheroid core to the outer tissue. Additionally, we showed the versatility of the technique across cancerous and noncancerous cell types, and tested its potential as a cancer diagnostic tool through the administration of drugs such as irinotecan, rotenone, and FCCP. Our technique successfully tracked the metabolic changes induced by each drug while reporting on the spatial

https://doi.org/10.1021/cbmi.4c00105
Chem. Biomed. Imaging 2025, 3, 310−321

location of the ROS activity. In our system, we implicate hydrogen peroxide because of its relative stability, the light generated in the positive control, and the enhanced ECL intensity generated in cells exposed to irinotecan, a known hydrogen peroxide upregulator. While the technique still has limitations, such as its inability to provide cellular resolution or to probe individual components of cellular pathways that might upregulate hydrogen peroxide production, or to provide ECL images at different focal planes due to the one-time use nature of the ITO, the luminol-based ECL system reported here can be used as both a tool for cancer diagnosis and as a platform to study drug efficacy. These tools will have much wider applications in understanding the real-time propagation of human disease in systems that more closely relate to human tissue.

■ ASSOCIATED CONTENT

Supporting Information

The Supporting Information is available free of charge at https://pubs.acs.org/doi/10.1021/cbmi.4c00105.

Cyclic voltammograms, H_2O_2 calibration curve, and live−dead spheroid analysis (PDF)

■ AUTHOR INFORMATION

Corresponding Authors

Stefania Rapino − *Department of Chemistry "Giacomo Ciamician", University of Bologna, 40129 Bologna, Italy; IRCCS Azienda Ospedaliero-Universitaria di Bologna, 40138 Bologna, Italy;* orcid.org/0000-0001-6913-0119; Email: stefania.rapino3@unibo.it

Jeffrey E. Dick − *Department of Chemistry, Purdue University, West Lafayette, Indiana 47906, United States; Elmore Family School of Electrical and Computer Engineering, Purdue University, West Lafayette, Indiana 47906, United States;* orcid.org/0000-0002-4538-9705; Email: jdick@purdue.edu

Authors

Vanshika Gupta − *Department of Chemistry, Purdue University, West Lafayette, Indiana 47906, United States*

Francesco Falciani − *Department of Chemistry "Giacomo Ciamician", University of Bologna, 40129 Bologna, Italy*

Brady R. Layman − *Department of Chemistry, Purdue University, West Lafayette, Indiana 47906, United States;* orcid.org/0000-0002-8077-8490

Megan L. Hill − *Department of Chemistry, Purdue University, West Lafayette, Indiana 47906, United States;* orcid.org/0000-0001-6896-3426

Complete contact information is available at: https://pubs.acs.org/10.1021/cbmi.4c00105

Author Contributions

‖Denotes equal contribution for VG, FF, and BRL. The authors reserve the right to list the three names in any order for the three names. Conceptualization: VG, FF, BRL, JED. Methodology: VG, FF, BRL, JED. Formal Analysis: VG, FF, BRL. Investigation: VG, FF, BRL, MLH. Writing—Original Draft: VG, BRL. Writing—Review and Editing: VG, FF, BRL, MLH, JED. Visualization: VG, FF, BRL. Supervision: SR, JED. Funding Acquisition: JED.

Notes

The authors declare no competing financial interest.

■ ACKNOWLEDGMENTS

We would also like to acknowledge support from the National Institutes of Health under Grant No. R35-GM138133-01. Vanshika Gupta is supported by the National Science Foundation through the Graduate Research Fellowship Program (NSF-GRFP). Brady R. Layman is supported by the Department of Defense (DoD) through the National Defense Engineering Graduate (NDSEG) Fellowship. Megan L. Hill is supported by the Department of Energy (DOE) through the University Nuclear Leadership Program Graduate Fellowship (UNLP). We would like to thank Dane Wagner and Samuel Nortz for their helpful discussions.

■ REFERENCES

(1) Harrison, R. G. Observations on the Living Developing Nerve Fiber. *Proc. Soc. Exp. Biol. Med.* **1906**, *4* (1), 140.

(2) Calitz, C.; Pavlović, N.; Rosenquist, J.; Zagami, C.; Samanta, A.; Heindryckx, F. A Biomimetic Model for Liver Cancer to Study Tumor-Stroma Interactions in a 3d Environment with Tunable Bio-Physical Properties. *J. Visualized Exp.* **2020**, DOI: 10.3791/61606.

(3) Xiao, S.; Ahmed, W.; Mohsin, A.; Guo, M. Continuous Feeding Reduces the Generation of Metabolic Byproducts and Increases Antibodies Expression in Chinese Hamster Ovary-K1 Cells. *Life* **2021**, *11* (9), 945.

(4) Breslin, S.; O'Driscoll, L. The Relevance of Using 3D Cell Cultures, in Addition to 2D Monolayer Cultures, When Evaluating Breast Cancer Drug Sensitivity and Resistance. *Oncotarget* **2016**, *7* (29), 45745.

(5) Fitzgerald, A. A.; Li, E.; Weiner, L. M. 3D Culture Systems for Exploring Cancer Immunology. *Cancers* **2021**, *13*, 56.

(6) Chatzinikolaidou, M. Cell Spheroids: The New Frontiers in in Vitro Models for Cancer Drug Validation. *Drug Discovery Today* **2016**, *21*, 1553.

(7) Wolff, A.; Frank, M.; Staehlke, S.; Springer, A.; Hahn, O.; Meyer, J.; Peters, K. 3D Spheroid Cultivation Alters the Extent and Progression of Osteogenic Differentiation of Mesenchymal Stem/Stromal Cells Compared to 2D Cultivation. *Biomedicines* **2023**, *11* (4), 1049.

(8) Marques, I. A.; Fernandes, C.; Tavares, N. T.; Pires, A. S.; Abrantes, A. M.; Botelho, M. F. Magnetic-Based Human Tissue 3D Cell Culture: A Systematic Review. *International Journal of Molecular Sciences* **2022**, *23*, 12681.

(9) Li, S.; Yang, K.; Chen, X.; Zhu, X.; Zhou, H.; Li, P.; Chen, Y.; Jiang, Y.; Li, T.; Qin, X.; Yang, H.; Wu, C.; Ji, B.; You, F.; Liu, Y. Simultaneous 2D and 3D Cell Culture Array for Multicellular Geometry, Drug Discovery and Tumor Microenvironment Reconstruction. *Biofabrication* **2021**, *13* (4), 045013.

(10) Edwards, A. M.; Arrowsmith, C. H.; Bountra, C.; Bunnage, M. E.; Feldmann, M.; Knight, J. C.; Patel, D. D.; Prinos, P.; Taylor, M. D.; Sundström, M.; et al. Preclinical Target Validation Using Patient-Derived Cells. *Nat. Rev. Drug Discovery* **2015**, *14*, 149.

(11) Kimlin, L. C.; Casagrande, G.; Virador, V. M. In Vitro Three-Dimensional (3D) Models in Cancer Research: An Update. *Mol. Carcinog.* **2013**, *52* (3), 167.

(12) Baker, B. M.; Chen, C. S. Deconstructing the Third Dimension-How 3D Culture Microenvironments Alter Cellular Cues. *Journal of Cell Science* **2012**, DOI: 10.1242/jcs.079509.

(13) Riedl, A.; Schlederer, M.; Pudelko, K.; Stadler, M.; Walter, S.; Unterleuthner, D.; Unger, C.; Kramer, N.; Hengstschläger, M.; Kenner, L.; Pfeiffer, D.; Krupitza, G.; Dolznig, H. Comparison of Cancer Cells in 2D vs 3D Culture Reveals Differences in AKT-MTOR-S6K Signaling and Drug Responses. *J. Cell Sci.* **2016**, DOI: 10.1242/jcs.188102.

(14) Mehta, G.; Hsiao, A. Y.; Ingram, M.; Luker, G. D.; Takayama, S. Opportunities and Challenges for Use of Tumor Spheroids as Models to Test Drug Delivery and Efficacy. *J. Controlled Release* **2012**, *164* (2), 192.
(15) Wong, M. K.; Wahed, M.; Shawky, S. A.; Dvorkin-Gheva, A.; Raha, S. Transcriptomic and Functional Analyses of 3D Placental Extravillous Trophoblast Spheroids. *Sci. Rep.* **2019**, DOI: 10.1038/s41598-019-48816-8.
(16) Ivanov, D. P.; Parker, T. L.; Walker, D. A.; Alexander, C.; Ashford, M. B.; Gellert, P. R.; Garnett, M. C. Multiplexing Spheroid Volume, Resazurin and Acid Phosphatase Viability Assays for High-Throughput Screening of Tumour Spheroids and Stem Cell Neurospheres. *PLoS One* **2014**, *9*, e103817.
(17) Li, Y.; Luo, J.; Lin, M. T.; Zhi, P.; Guo, W. W.; Han, M.; You, J.; Gao, J. Q. Co-Delivery of Metformin Enhances the Antimultidrug Resistant Tumor Effect of Doxorubicin by Improving Hypoxic Tumor Microenvironment. *Mol. Pharm.* **2019**, *16* (7), 2966.
(18) Phillips, T. A.; Caprettini, V.; Aggarwal, N.; Marcotti, S.; Tetley, R.; Mao, Y.; Shaw, T.; Chiappini, C.; Parsons, M.; Cox, S. A Method for Reproducible High-Resolution Imaging of 3D Cancer Cell Spheroids. *J. Microsc.* **2023**, *291* (1), 30.
(19) Tanaka, S.; Takizawa, K.; Nakamura, F. One-Step Visualization of Natural Cell Activities in Non-Labeled Living Spheroids. *Sci. Rep* **2022**, DOI: 10.1038/s41598-022-05347-z.
(20) Alzeeb, G.; Dubreuil, M.; Arzur, D.; Rivet, S.; Corcos, L.; Grand, Y. Le; Le Jossic-Corcos, C. Gastric Cancer Multicellular Spheroid Analysis by Two-Photon Microscopy. *Biomed. Opt. Express* **2022**, *13* (5), 3120.
(21) Karrobi, K.; Tank, A.; Fuzail, M. A.; Kalidoss, M.; Tilbury, K.; Zaman, M.; Ferruzzi, J.; Roblyer, D. Fluorescence Lifetime Imaging Microscopy (FLIM) Reveals Spatial-Metabolic Changes in 3D Breast Cancer Spheroids. *Sci. Rep.* **2023**, DOI: 10.1038/s41598-023-30403-7.
(22) Rane, T. D.; Armani, A. M. Two-Photon Microscopy Analysis of Gold Nanoparticle Uptake in 3D Cell Spheroids. *PLoS One* **2016**, *11* (12), e0167548.
(23) David, B. P.; Dubrovskyi, O.; Speltz, T. E.; Wolff, J. J.; Frasor, J.; Sanchez, L. M.; Moore, T. W. Using Tumor Explants for Imaging Mass Spectrometry Visualization of Unlabeled Peptides and Small Molecules. *ACS Med. Chem. Lett.* **2018**, *9* (7), 768.
(24) Xia, D.; Jin, R.; Pan, R.; Chen, H. Y.; Jiang, D. In Situ Spatial Analysis of Metabolic Heterogeneity in Single Living Tumor Spheroids Using Nanocapillary-Based Electrospray Ionization Mass Spectroscopy. *Anal. Chem.* **2023**, *95* (27), 10221.
(25) Robertson, J. B.; Davis, C. R.; Johnson, C. H. Visible Light Alters Yeast Metabolic Rhythms by Inhibiting Respiration. *Proc. Natl. Acad. Sci. U. S. A.* **2013**, *110* (52), 21130.
(26) Yin, L.; Wang, W.; Wang, S.; Zhang, F.; Zhang, S.; Tao, N. How Does Fluorescent Labeling Affect the Binding Kinetics of Proteins with Intact Cells? *Biosens. Bioelectron.* **2015**, *66*, 412.
(27) Avard, R. C.; Broad, M. L.; Zandkarimi, F.; Devanny, A. J.; Hammer, J. L.; Yu, K.; Guzman, A.; Kaufman, L. J. DISC-3D: Dual-Hydrogel System Enhances Optical Imaging and Enables Correlative Mass Spectrometry Imaging of Invading Multicellular Tumor Spheroids. *Sci. Rep.* **2023**, DOI: 10.1038/s41598-023-38699-1.
(28) Chen, P.; Han, Y.; Wang, L.; Zheng, Y.; Zhu, Z.; Zhao, Y.; Zhang, M.; Chen, X.; Wang, X.; Sun, C. Spatially Resolved Metabolomics Combined with the 3D Tumor-Immune Cell Coculture Spheroid Highlights Metabolic Alterations during Anti-tumor Immune Response. *Anal. Chem.* **2023**, *95* (41), 15153.
(29) Li, H.; Hummon, A. B. Imaging Mass Spectrometry of Three-Dimensional Cell Culture Systems. *Anal. Chem.* **2011**, *83* (22), 8794.
(30) Utagawa, Y.; Ino, K.; Shinoda, Y.; Yamazaki, M.; Abe, H.; Shiku, H. Enzyme-Free In-Situ Electrochemical Measurement Using a Porous Membrane Electrode for Glucose Transport into Cell Spheroids. *ACS Sens* **2024**, *9* (8), 4248−4255.
(31) Hiramoto, K.; Komatsu, K.; Shikuwa, R.; Konno, A.; Sato, Y.; Hirano-Iwata, A.; Ino, K.; Shiku, H. Evaluation of Respiratory and Secretory Activities of Multicellular Spheroids via Electrochemiluminescence Imaging. *Electrochim. Acta* **2023**, *458*, 142507.
(32) Bouffier, L.; Sojic, N. Chapter 1: Introduction and Overview of Electrogenerated Chemiluminescence. *RSC Detection Sci.* **2019**, 1.
(33) Zanut, A.; Fiorani, A.; Canola, S.; Saito, T.; Ziebart, N.; Rapino, S.; Rebeccani, S.; Barbon, A.; Irie, T.; Josel, H. P.; Negri, F.; Marcaccio, M.; Windfuhr, M.; Imai, K.; Valenti, G.; Paolucci, F. Insights into the Mechanism of Coreactant Electrochemiluminescence Facilitating Enhanced Bioanalytical Performance. *Nat. Commun.* **2020**, DOI: 10.1038/s41467-020-16476-2.
(34) Ma, Y.; Colin, C.; Descamps, J.; Arbault, S.; Sojic, N. Shadow Electrochemiluminescence Microscopy of Single Mitochondria. *Angew. Chem. Int. Ed.* **2021**, *60* (34), 18742.
(35) Han, D.; Yang, M.; Feng, Z.; Wu, Y.; Sojic, N.; Jiang, D. Thickness-Resolved Electrochemiluminescence Microscopy of Extracellular Matrix at Tumor Tissues for Rapid Cancer Diagnosis. *ACS Appl. Mater. Interfaces* **2024**, *16* (25), 32078−32086.
(36) Layman, B. R.; Dick, J. E. Through-Space Electrochemiluminescence Reveals Bubble Forces at Remote Phase Boundaries. *J. Am. Chem. Soc.* **2024**, *146* (1), 707−713.
(37) Layman, B. R.; Dick, J. E. Phase-Resolved Electrochemiluminescence with a Single Luminophore. *J. Phys. Chem. Lett.* **2023**, *14* (36), 8151−8156.
(38) Knežević, S.; Totoricaguena-Gorriño, J.; Gajjala, R. K. R.; Hermenegildo, B.; Ruiz-Rubio, L.; Vilas-Vilela, J. L.; Lanceros-Méndez, S.; Sojic, N.; Del Campo, F. J. Enhanced Electrochemiluminescence at the Gas/Liquid Interface of Bubbles Propelled into Solution. *J. Am. Chem. Soc.* **2024**, *146* (32), 22724−22735.
(39) Fu, Y.; Xie, B.; Liu, M.; Hou, S.; Zhu, Q.; Kuhn, A.; Zhang, L.; Yang, W.; Sojic, N. Bipolar Electrochemiluminescence at the Water/Organic Interface. *Chem. Sci.* **2024**, *15* (47), 19907−19912.
(40) Herchenbach, P. J.; Layman, B. R.; Dick, J. E. Quantifying the Interfacial Tension of Adsorbed Droplets on Electrified Interfaces. *J. Colloid Interface Sci.* **2024**, *674*, 474−481.
(41) Voci, S.; Goudeau, B.; Valenti, G.; Lesch, A.; Jović, M.; Rapino, S.; Paolucci, F.; Arbault, S.; Sojic, N. Surface-Confined Electrochemiluminescence Microscopy of Cell Membranes. *J. Am. Chem. Soc.* **2018**, *140* (44), 14753.
(42) Valenti, G.; Scarabino, S.; Goudeau, B.; Lesch, A.; Jović, M.; Villani, E.; Sentic, M.; Rapino, S.; Arbault, S.; Paolucci, F.; Sojic, N. Single Cell Electrochemiluminescence Imaging: From the Proof-of-Concept to Disposable Device-Based Analysis. *J. Am. Chem. Soc.* **2017**, *139* (46), 16830.
(43) Layman, B. R.; Dick, J. E. Electroprecipitating the Sulfate Radical Anion Amplifies Electrochemiluminescence in Space and Time. *J. Am. Chem. Soc.* **2024**, *146* (38), 26216−26222.
(44) Zhao, Y.; Descamps, J.; Léger, Y.; Sojic, N.; Loget, G. Light Conversion by Electrochemiluminescence at Semiconductor Surfaces. *Acc. Chem. Res.* **2024**, *57* (15), 2144−2153.
(45) Arias-Aranda, L. R.; Salinas, G.; Kuhn, A.; Xu, G.; Kanoufi, F.; Bouffier, L.; Sojic, N. Complex Electrochemiluminescence Patterns Shaped by Hydrodynamics at a Rotating Bipolar Electrode. *Chem. Sci.* **2024**, *15* (23), 8723−8730.
(46) Dong, J.; Lu, Y.; Xu, Y.; Chen, F.; Yang, J.; Chen, Y.; Feng, J. Direct Imaging of Single-Molecule Electrochemical Reactions in Solution. *Nature* **2021**, *596* (7871), 244.
(47) Knežević, S.; Han, D.; Liu, B.; Jiang, D.; Sojic, N. Electrochemiluminescence Microscopy. *Angew. Chem., Int. Ed.* **2024**, *63* (29), No. e202407588.
(48) Rebeccani, S.; Zanut, A.; Santo, C. I.; Valenti, G.; Paolucci, F. A Guide Inside Electrochemiluminescent Microscopy Mechanisms for Analytical Performance Improvement. *Anal. Chem.* **2022**, *94*, 336.
(49) Gao, H.; Han, W.; Qi, H.; Gao, Q.; Zhang, C. Electrochemiluminescence Imaging for the Morphological and Quantitative Analysis of Living Cells under External Stimulation. *Anal. Chem.* **2020**, *92* (12), 8278.
(50) Zhou, P.; Hu, S.; Guo, W.; Su, B. Deciphering Electrochemiluminescence Generation from Luminol and Hydrogen

Peroxide by Imaging Light Emitting Layer. *Fundamental Research* **2022**, *2* (5), 682−687.
(51) Mariani, C.; Bogialli, S.; Paolucci, F.; Pastore, P.; Zanut, A.; Valenti, G. Enhancing Electrochemiluminescence Intensity through Emission Layer Control. *Electrochim. Acta* **2024**, *489*, 144256.
(52) Li, H.; Zhou, H.; Zhang, T.; Zhang, Z.; Zhao, G.; Wang, C. Electrocatalytic Generation of Cathodic Luminol Electrochemiluminescence with Carbonized Polydopamine Nanotubes at a Low Positive Potential. *ACS Sustain. Chem. Eng.* **2022**, *10* (31), 10361.
(53) Sies, H.; Belousov, V. V.; Chandel, N. S.; Davies, M. J.; Jones, D. P.; Mann, G. E.; Murphy, M. P.; Yamamoto, M.; Winterbourn, C. Defining Roles of Specific Reactive Oxygen Species (ROS) in Cell Biology and Physiology. *Nat. Rev. Mol. Cell Biol.* **2022**, *23* (7), 499−515.
(54) Sies, H.; Jones, D. P. Reactive Oxygen Species (ROS) as Pleiotropic Physiological Signalling Agents. *Nat. Rev. Mol. Cell Biol.* **2020**, *21*, 363.
(55) Zhang, W.; Li, Y.; Ding, H.; Du, Y.; Wang, L. Hydrogen Peroxide Prevents Vascular Calcification Induced ROS Production by Regulating Nrf-2 Pathway. *Ren. Fail* **2016**, *38* (7), 1099.
(56) Shin, J. Y.; Park, J.; Jang, H. K.; Lee, T. J.; La, W. G.; Bhang, S. H.; Kwon, I. K.; Kwon, O. H.; Kim, B. S. Efficient Formation of Cell Spheroids Using Polymer Nanofibers. *Biotechnol. Lett.* **2012**, *34* (5), 795.
(57) Calabria, D.; Lazzarini, E.; Pace, A.; Trozzi, I.; Zangheri, M.; Cinti, S.; Difonzo, M.; Valenti, G.; Guardigli, M.; Paolucci, F.; Mirasoli, M. Smartphone-Based 3D-Printed Electrochemiluminescence Enzyme Biosensor for Reagentless Glucose Quantification in Real Matrices. *Biosens. Bioelectron.* **2023**, *227*, 115146.
(58) Kim, M.; Yun, H. W.; Park, D. Y.; Choi, B. H.; Min, B. H. Three-Dimensional Spheroid Culture Increases Exosome Secretion from Mesenchymal Stem Cells. *Tissue Eng. Regen. Med.* **2018**, *15* (4), 427.
(59) Cui, L.; Zhao, M. H.; Li, C. C.; Wang, Q.; Luo, X.; Zhang, C. Y. A Host-Guest Interaction-Based and Metal-Organic Gel-Based Biosensor with Aggregation-Induced Electrochemiluminescence Enhancement for Methyltransferase Assay. *Anal. Chem.* **2021**, *93* (5), 2974.
(60) Wartenberg, M.; Fischer, K.; Hescheler, J.; Sauer, H. Redox Regulation of P-Glycoprotein-Mediated Multidrug Resistance in Multicellular Prostate Tumor Spheroids. *Int. J. Cancer* **2000**, *85* (2), 267.
(61) Ivascu, A.; Kubbies, M. Diversity of Cell-Mediated Adhesions in Breast Cancer Spheroids. *Int. J. Oncol.* **2007**, DOI: 10.3892/ijo.31.6.1403.
(62) Singh, K.; Gautam, P. K. Macrophage Infiltration in 3D Cancer Spheroids to Recapitulate the TME and Unveil Interactions within Cancer Cells and Macrophages to Modulate Chemotherapeutic Drug Efficacy. *BMC Cancer* **2023**, DOI: 10.1186/s12885-023-11674-9.
(63) Takahashi, N.; Cho, P.; Selfors, L. M.; Kuiken, H. J.; Kaul, R.; Fujiwara, T.; Harris, I. S.; Zhang, T.; Gygi, S. P.; Brugge, J. S. 3D Culture Models with CRISPR Screens Reveal Hyperactive NRF2 as a Prerequisite for Spheroid Formation via Regulation of Proliferation and Ferroptosis. *Mol. Cell* **2020**, *80* (5), 828.
(64) Iansante, V.; Choy, P. M.; Fung, S. W.; Liu, Y.; Chai, J. G.; Dyson, J.; Del Rio, A.; D'Santos, C.; Williams, R.; Chokshi, S.; Anders, R. A.; Bubici, C.; Papa, S. PARP14 Promotes the Warburg Effect in Hepatocellular Carcinoma by Inhibiting JNK1-Dependent PKM2 Phosphorylation and Activation. *Nat. Commun.* **2015**, DOI: 10.1038/ncomms8882.
(65) van Noorden, C. J. F.; Yetkin-Arik, B.; Serrano Martinez, P.; Bakker, N.; van Breest Smallenburg, M. E.; Schlingemann, R. O.; Klaassen, I.; Majc, B.; Habic, A.; Bogataj, U.; Galun, S. K.; Vittori, M.; Erdani Kreft, M.; Novak, M.; Breznik, B.; Hira, V. V. V. New Insights in ATP Synthesis as Therapeutic Target in Cancer and Angiogenic Ocular Diseases. *Journal of Histochemistry & Cytochemistry* **2024**, *72* (5), 329−352.
(66) Cunningham, D.; Maroun, J.; Vanhoefer, U.; Van Cutsem, E. Optimizing the Use of Irinotecan in Colorectal Cancer. *Oncologist* **2001**, *6* (S4), 17.
(67) Vanhoefer, U.; Harstrick, A.; Achterrath, W.; Cao, S.; Seeber, S.; Rustum, Y. M. Irinotecan in the Treatment of Colorectal Cancer: Clinical Overview. *Journal of Clinical Oncology* **2001**, *19*, 1501.
(68) Xu, Y.; Villalona-Calero, M. A. Irinotecan: Mechanisms of Tumor Resistance and Novel Strategies for Modulating Its Activity. *Annals of Oncology* **2002**, *13*, 1841.
(69) He, J.; Zhou, C.; Xu, X.; Zhou, Z.; Danoy, M.; Shinohara, M.; Xiao, W.; Zhu, D.; Zhao, X.; Feng, X.; Mao, Y.; Sun, W.; Sakai, Y.; Yang, H.; Pang, Y. Scalable Formation of Highly Viable and Functional Hepatocellular Carcinoma Spheroids in an Oxygen-Permeable Microwell Device for Anti-Tumor Drug Evaluation. *Adv. Healthc. Mater.* **2022**, DOI: 10.1002/adhm.202200863.
(70) Zheng, J.; Yan, X.; Lu, T.; Song, W.; Li, Y.; Liang, J.; Zhang, J.; Cai, J.; Sui, X.; Xiao, J.; Chen, H.; Chen, G.; Zhang, Q.; Liu, Y.; Yang, Y.; Zheng, K.; Pan, Z. CircFOXK2 Promotes Hepatocellular Carcinoma Progression and Leads to a Poor Clinical Prognosis via Regulating the Warburg Effect. *J. Exp. Clin. Cancer Res.* **2023**, DOI: 10.1186/s13046-023-02624-1.
(71) Vander Heiden, M. G.; Cantley, L. C.; Thompson, C. B. Understanding the Warburg Effect: The Metabolic Requirements of Cell Proliferation. *Science* **2009**, *324*, 1029.
(72) El-Sheikh, P.; Shamloula, M.; Atef, A.; El-Guindy, D. Evaluation of Pyruvate Kinase M2 (PKM2) and Epidermal Growth Factor Receptor (EGFR) Expression and Their Clinicopathologic Significance in Bladder Urothelial Carcinoma. *International Journal of Cancer and Biomedical Research* **2021**, *0*, 0.
(73) Li, R.; Wang, Y.; Zhu, L.; Zhang, X.; Liu, D.; Li, Q.; Ni, B.; Hu, L.; Zhang, Z.; Zhang, Y.; Wang, X.; Jiang, S.-H. A Positive Feedback between HIF1α and Lysyl Oxidase-like 2 Dictates the Warburg Effect in Pancreatic Cancer. *Res. Square* **2021**, DOI: 10.21203/rs.3.rs-360740/v1.
(74) Dubois, C.; Dufour, R.; Daumar, P.; Aubel, C.; Szczepaniak, C.; Blavignac, C.; Mounetou, E.; Penault-Llorca, F.; Bamdad, M. Development and Cytotoxic Response of Two Proliferative MDAMB-231 and Non-Proliferative SUM1315 Three-Dimensional Cell Culture Models of Triple-Negative Basal-like Breast Cancer Cell Lines. *Oncotarget* **2017**, *8* (56), 95316.
(75) Theodossiou, T. A.; Wälchli, S.; Olsen, C. E.; Skarpen, E.; Berg, K. Deciphering the Nongenomic, Mitochondrial Toxicity of Tamoxifens As Determined by Cell Metabolism and Redox Activity. *ACS Chem. Biol.* **2016**, *11* (1), 251.
(76) Qing, Y.; Xiang, X.; Li, S.; Wang, M.; Liang, Z.; Ren, J. Integrated Evaluation the Antioxidant Activity of Epicatechin from Cell Dynamics. *Biotechnol. Prog.* **2023**, DOI: 10.1002/btpr.3328.
(77) Wanandi, S. I.; Hardiany, N. S.; Siregar, N. C.; Sadikin, M. Suppression of Manganese Superoxide Dismutase Activity in Rotenone-Treated Human Glioblastoma T98G Cells Reduces Cell Viability. *Asian J. Pharm. Clin. Res.* **2018**, *11* (1), 48.
(78) Dempwolff, F.; Reimold, C.; Reth, M.; Graumann, P. L. Bacillus Subtilis MreB Orthologs Self-Organize into Filamentous Structures underneath the Cell Membrane in a Heterologous Cell System. *PLoS One* **2011**, *6* (11), e27035.
(79) Teixeira, J.; Basit, F.; Swarts, H. G.; Forkink, M.; Oliveira, P. J.; Willems, P. H. G. M.; Koopman, W. J. H. Extracellular Acidification Induces ROS- and MPTP-Mediated Death in HEK293 Cells. *Redox Biol.* **2018**, *15*, 394.
(80) Yu, Y. X.; Li, Y. P.; Gao, F.; Hu, Q. S.; Zhang, Y.; Chen, D.; Wang, G. H. Vitamin K2 Suppresses Rotenone-Induced Microglial Activation in Vitro. *Acta Pharmacol. Sin.* **2016**, *37* (9), 1178.

https://doi.org/10.1021/cbmi.4c00105
Chem. Biomed. Imaging 2025, 3, 310−321